Journal of Materials Chemistry C

ROYAL SOCIETY OF CHEMISTRY

PAPER

View Article Online
View Journal | View Issue

Cite this: J. Mater. Chem. C, 2024, 12, 2814

Efficient and stable near-infrared $Y_2Mg_2Al_2Si_2O_{12}:Cr^{3+}$ phosphor: analysis of the luminescence source by a site elimination strategy†

Yixin Sun,[a] Mengmeng Shang, *[a] Yining Wang,[a] Yiying Zhu,[a] Xiaole Xing,[a] Peipei Dang[b] and Jun Lin *[b]

Received 17th November 2023,
Accepted 17th January 2024

DOI: 10.1039/d3tc04245f

rsc.li/materials-c

Near-infrared (NIR) phosphor-converted light-emitting diodes (pc-LEDs) are the ideal light source for next-generation NIR spectroscopy, and developing novel NIR phosphors with high performance is crucial to achieve a wide range of NIR pc-LED applications. In this work, NIR luminescent material $Y_2Mg_2Al_2Si_2O_{12}$ (YMAS):2%Cr^{3+} with good quantum efficiency (79%) and excellent thermal stability (88%@100 °C) is prepared. Under 430 nm light excitation, YMAS:2%Cr^{3+} emits 620–1100 nm NIR light with a full-width at half maximum (FWHM) of 153 nm. Fluorescence decay curves, photoluminescence (PL) spectra, 7 K PL spectra, the Rietveld refinement, ^{27}Al solid-state nuclear magnetic resonance (ss-NMR) spectra and time-resolved emission spectroscopy (TRS) confirm that Cr^{3+} has two different luminescence centers in the YMAS lattice. Benefiting from the site elimination strategy, the double luminescence centers are proven to be derived from Cr^{3+} ions occupying the two sites [Al_1O_6] and [Al_2O_4]. The NIR packaging device prepared using YMAS:2%Cr^{3+} has outstanding NIR output power and photovoltaic conversion efficiency as high as 45.7 mW@100 mA and 16.7%@100 mA, respectively. Owing to the excellent performance of the YMAS:2%Cr^{3+} sample, it presents excellent practical performance in plant growth, bioimaging, non-destructive testing and night vision.

1. Introduction

As an integral part of the electromagnetic spectrum, broadband NIR light plays an unprecedentedly important role in biological detection, laboratory instrumentation, chemical industry, optoelectronic devices, and medical diagnostics.[1–6] In particular, NIR light in the 700–1100 nm region is known as the first biological window, which can be used in bio-imaging and non-destructive testing due to its considerable penetration depth in biological tissues besides plant growth and night vision application.[7–9] Traditional NIR light sources such as incandescent lamps and halogen lamps have a series of problems like large size, low output, and high energy consumption, which hinder the further development of portable and integrated NIR technology. And the GaAs(Al/In)-based NIR LEDs are more competitive with the advantages of high efficiency and long lifetime. But their narrow FWHM (less than 50 nm) and high price limit their application. NIR pc-LEDs offer extraordinary advantages over other conventional light sources in terms of low power consumption, small size for easy integration, eco-friendliness, durability and long lifetime.[10–12] NIR pc-LEDs are fabricated to coat NIR phosphors on the LED chip or the package wall. The NIR phosphor as a critical component of pc-LEDs affects the overall luminescence performance and emission spectra of the devices. However, for a long time, research studies on solid luminescent materials have mainly focused on visible and ultraviolet light-emitting materials. There is no corresponding mature NIR phosphor product on the market, and further research and development are urgently needed.

[a] Key Laboratory for Liquid–Solid Structural Evolution and Processing of Materials Ministry of Education, School of Material Science and Engineering, Shandong University, 17923 Jingshi Road, Jinan 250061, P. R. China.
E-mail: mmshang@sdu.edu.cn

[b] State Key Laboratory of Rare Earth Resource Utilization, Changchun Institute of Applied Chemistry, Chinese Academy of Sciences, Changchun 130022, P. R. China.
E-mail: jlin@ciac.ac.cn

† Electronic supplementary information (ESI) available: Main parameters of processing and refinement results of $Y_2Mg_{2-y}Al_{2+2y}Si_{2-y}O_{12}$:2%$Cr^{3+}$ (y = 0 and 1). The calculated average lifetime of YMAS:$x$$Cr^{3+}$ (x = 1–22%) and YMA_4S:$x$$Cr^{3+}$ (x = 2–15%). The content of each element in YMA_4S:2%Cr^{3+}. The SEM image and quantum yield diagram of YMAS:2%Cr^{3+}. And the PL spectra of YMAS:$x$$Cr^{3+}$ (x = 2% and 22%) at 7 K. Tanabe-Sugano diagram for Cr^{3+} ion in octahedral coordination and tetrahedral coordination. XRD patterns of $Y_2Mg_{2-y}Al_{2+2y}Si_{2-y}O_{12}$:2%$Cr^{3+}$($y$ = 0.1, 0.5 and 1). Rietveld refinement of YMAS:2%Cr^{3+} and YMA_4S:2%Cr^{3+}. ^{27}Al ss-NMR spectra of YMAS:$x$$Cr^{3+}$ (x = 0 and 22%). Temperature-dependent PL spectra and integral intensity of $Y_2Mg_{2-y}Al_{2+2y}Si_{2-y}O_{12}$:2%$Cr^{3+}$($y$ = 1, 0.1, 0.5, 0.9 and 1). The Kubelka–Munk formula. See DOI: https://doi.org/10.1039/d3tc04245f

Table 1 Summary of the main properties of Cr^{3+}-doped luminescent materials

Phosphor	λ_{em} (nm)	FWHM (nm)	IQE (%)	$I_{150°C}$ (%)	Output power (100 mA)	Efficiency (100 mA)	Ref.
$LiInSi_2O_6:Cr^{3+}$	840	143	75	77	51.6 mW	17.2%	17
$ScBO_3:Cr^{3+}$	800	120	65	51	26 mW	7%	16
$NaScSi_2O_6:Cr^{3+}$	860	156	22.2	69	203 mW@300 mA	5.7%@300 mA	18
$SrGa_{12}O_{19}:Cr^{3+}$	750	100	82.4	—	—	—	19
$Sr_2ScSbO_6:Cr^{3+}$	890	130	82	66	—	—	20
$Ca_3Sc_2Si_3O_{12}:Cr^{3+}$	770	110	92.3	97.4	97.8 mW@520 mA	64.7%@520 mA	15
$CaLu_2Mg_2Si_3O_{12}:Cr^{3+}$	765	120	~41	82.3	34.75 mW	11.6%	13
$Y_2Mg_2Ga_2Si_2O_{12}:Cr^{3+}$	790	180	44.3	70@100 °C	14 mW	5%	21
$Ca_2LuScAl_2Si_2O_{12}:Cr^{3+}$	752	142	73.7	76	24.59 mW	8.22%	22
$Y_2Mg_2Al_2Si_2O_{12}:Cr^{3+}$	750	153	79	89@100 °C	45.7 mW	16.7%	This work

The core of the NIR luminescent material is the activator, which determines the intrinsic electron-transition mechanism of luminescent materials. Cr^{3+} ions are one of the most favored NIR emission activators because of their tunable broadband and efficient NIR emissions, such as $CaLu_2Mg_2Si_3O_{12}:Cr^{3+}$,[13] $K_2SrGe_8O_{18}:Cr^{3+}$,[14] $Ca_3Sc_2Si_3O_{12}:Cr^{3+}$,[15] and $ScBO_3:Cr^{3+}$.[16] Among them, garnet-type compounds are rich in a variety of cationic sites, which are suitable for Cr^{3+} doping, and Cr^{3+} doped garnet structure NIR phosphors have attracted much attention due to their variable composition, adjustable spectrum, high quantum efficiency and good thermal stability, as listed in Table 1.

In this work, a novel $Y_2Mg_2Al_2Si_2O_{12}$ (YMAS):Cr^{3+} NIR phosphor with garnet structure is reported for the first time. There are three suitable sites for Cr^{3+} occupation in the YMAS lattice, *i.e.* $[AlO_6]$ octahedron, $[MgO_6]$ octahedron and $[AlO_4]$ tetrahedron. The optimized YMAS:2%Cr^{3+} phosphor has a broadband NIR emission of 620–1100 nm (the peak at 750 nm and FWHM of 153 nm). A site elimination strategy is proposed to eliminate the $[MgO_6]$ octahedral sites by introducing $[Al^{3+}$–$Al^{3+}]$ ion pairs in place of $[Mg^{2+}$–$Si^{4+}]$ without drastic structural changes, which verifies the dual luminescence centers (Cr^{3+} in the $[AlO_6]$ octahedron and $[AlO_4]$ tetrahedron) of Cr^{3+}. And the detailed PL mechanism is discussed in this paper. Moreover, YMAS:2%Cr^{3+} has excellent internal quantum efficiency (79%) and thermal stability (≈88%@100 °C). The NIR packaged device prepared from YMAS:2%Cr^{3+} and 460 nm chip has NIR output power and photovoltaic conversion efficiency of up to 45.7 mW@100 mA and 16.7%@100 mA, respectively. Due to the outstanding performance of the YMAS:2%Cr^{3+} sample, it is a potential candidate for practical applications in the field of plant growth, bioimaging, non-destructive testing and night vision.

2. Experimental section

2.1. Materials and synthesis

Powder samples with compositions of $Y_2Mg_2Al_2Si_2O_{12}$ (YMAS):$x$$Cr^{3+}$ (x = 0–30%), $Y_2Mg_{2-y}Al_{2+2y}Si_{2-y}O_{12}$:2%$Cr^{3+}$ (y = 0–1) and $Y_2MgAl_4SiO_{12}$ (YMA_4S):$z$$Cr^{3+}$ (z = 0–20%) were synthesized by a high-temperature solid state reaction. The raw materials Y_2O_3 (99.99%, Sinopharm Chemical Reagent Co.), MgO (98.5%, Sinopharm Chemical Reagent Co.), Al_2O_3 (99.99%, Sinopharm Chemical Reagent Co.), SiO_2 (99%, Sinopharm Chemical Reagent Co.), and Cr_2O_3 (99.95%, Aladdin) were weighed according to the stoichiometric amounts and then ground in an agate mortar for 30 min. Subsequently, the powder mixture was transferred into an alumina crucible and sintered at 1400 °C for 5–6 h in air. Finally, the as-prepared phosphors were cooled down to room temperature (RT) and ground into fine powders for subsequent testing.

2.2. NIR pc-LED fabrication

The as-prepared NIR phosphors were first mixed with epoxy resins (the mass ratio of the phosphor to the resin is fixed at 1 : 1) and then coated on the 460 nm GaN blue chips with 1 W power. The mixtures were cured at 120 °C for 1 h to form the final LED devices.

2.3. Characterization

The absorption spectra were recorded using a UV-vis-NIR spectrophotometer equipped with an integrating sphere (Cary 5000). The composition and phase purity of products were studied by powder X-ray diffraction (XRD) measurements using a D8 Focus diffractometer (Bruker) with Cu Kα radiation (λ = 0.15405 nm). The general structure analysis system program was used to conduct the structure refinements. The morphology and elemental composition were determined using a field emission scanning electron microscope (FESEM, S4800, Hitachi) equipped with an energy-dispersive spectrometer (EDS). The diffuse reflectance (DR) spectra were recorded using a UV-2600 LabSolutions UV-Vis spectrophotometer. The PL, PLE spectra, decay curves, TRS, 7 K spectra and temperature-dependent PL spectra (25–200 °C) were recorded using an Edinburgh fluorescence spectrometer (FLS1000) equipped with a continuous 450 W Xenon lamp as the steady-state excitation source, a pulsed high energy xenon flash lamp (μF2) as the transient excitation source, and a heating stage (TAP-02) as the temperature-controlled stage. The ^{27}Al solid-state nuclear magnetic resonance (ss-NMR) spectra were recorded on a Bruker Avance Neo 400WB. The photoluminescence quantum yield (QY) analysis was performed on an absolute PL quantum yield measurement system (C9920-02, Hamamatsu Photonics K.K., Japan). The optical properties of the NIR pc-LED devices were measured on a HAAS 2000 photoelectric measuring system from EVER FINE. The inductively coupled plasma mass spectrometry (ICP-MS) was performed on an Agilent 5110 (OES).

3. Results and discussion

3.1. Phase and crystal structure

The X-ray diffraction (XRD) patterns of prepared YMAS:xCr^{3+} (x = 0, 2% and 22%) are presented in Fig. 1a. The diffraction peaks of all the samples are in concordance with the standard data of $Y_3Al_5O_{12}$ (PDF #33-0040), indicating that garnet-type YMAS is successfully synthesized and the doping of Cr^{3+} ions does not obviously change the structure of the host. Fig. 1b shows the crystal structure of YMAS. Similar to $Y_3Al_5O_{12}$,[23] it can be viewed as a dense connection network composed of dodecahedrons, octahedrons and tetrahedrons. In YMAS, the octahedral cationic sites are occupied by Al1 and Mg1 atoms forming [Al1/Mg1O_6] octahedrons, [Al2/SiO_4] tetrahedrons are constructed by Al2 and Si atoms to form tetrahedral sites, and the dodecahedral cationic sites are composed of [Y/Mg2O_8] dodecahedrons. Through oxygen atoms, the [Al1/Mg1O_6] octahedron is connected to [Al2/SiO_4] with a shared corner and connected to [Y/Mg2O_8] with a shared edge. The activator ion Cr^{3+} (0.615 Å, CN = 6; 0.46 Å, CN = 4) tends to occupy octahedron and tetrahedron sites (compared to the dodecahedrons) due to the fact that it is more stable in an environment of coordination where the crystal field stabilization energy is stronger.[24–28] Combining the principle of similar ion radius and valence state shows that there are three types of cation sites in YMAS suitable for Cr^{3+} ions to occupy and form luminescent centers, which are Al1 (0.535 Å, CN = 6), Al2 (0.39 Å, CN = 4) and Mg1 (0.72 Å, CN = 6), respectively. This issue of site occupancy will be further discussed in the section on the PL properties and site elimination sections.

The morphology characterization of the scanning electron microscopy (SEM) and the elemental distribution of the energy-dispersive spectrometer (EDS) are illustrated in Fig. S1 (ESI†). The YMAS:Cr^{3+} product consists of non-uniform, micron-sized, and irregularly shaped particles. The elements Y, Mg, Al, Si, O and Cr are uniformly distributed throughout the specimen, indicating the successful doping of Cr^{3+} ions.

3.2. Photoluminescence properties

The diffuse reflection (DR) spectra of YMAS:xCr^{3+} (x = 0, 2%) are shown in Fig. 2a. There is almost no observable absorption in the visible region for YMAS, which means that a wide band gap can be expected. The optical band gap (E_g) can be calculated using the Kubelka–Munk formula[29,30] (eqn (S1) and (S2), ESI†), and the calculated E_g of YMAS is 5.87 eV (inset of Fig. 2a). The DR spectrum of YMAS:2%Cr^{3+} presents two strong absorption bands with peaks at 430 nm (blue region) and 600 nm (red region), and it also has a weak absorption at 690 nm, which is attributed to the $^4A_{2g} \rightarrow {}^2E_g$ transition of Cr^{3+} ions. In addition, the characteristic absorption band of Cr^{4+} ions at 850–1200 nm from the $^3A_2 \rightarrow {}^3T_2$ (^{3}F) transition is not observed,[31,32] which means that only Cr^{3+} exists in the samples (it should be noted that the breakover at 850–1200 nm is caused by instrument parameters).

Fig. 2b shows the photoluminescence excitation (PLE) and PL spectra of the YMAS:2%Cr^{3+} sample. The PLE spectrum has two broad bands in the blue (430 nm) and red (600 nm) spectral regions, which is consistent with the DR spectrum. Upon 430 nm light excitation, a broad NIR emission band (620–1100 nm, FWHM = 153 nm) is observed for YMAS:2%Cr^{3+}. In addition, it can be found that the shape of the emission spectra changes with different excitation wavelengths (392, 430, and 600 nm). All the emission spectra are composed of R line ($^2E_g \rightarrow {}^4A_{2g}$) and broadband emission, but the ratio of R line to broadband is significantly different. Apparently, the 392 nm light excitation favors R-line emission for the same doping concentration. The change in the emission spectra with excitation wavelength means that there may be multiple luminescent centers in the YMAS:Cr^{3+} sample. For more intuitive observation, the PL mapping spectrum of YMAS:2%Cr^{3+} is measured, as shown in Fig. 2c. Two sharp peak emissions at 690 nm and 710 nm and a broadband emission dominated by 800 nm are observed, which also proves multiple luminescent centers in the spectrum.

The normalized PL spectra (Fig. 2d) of YMAS:xCr^{3+}(x = 1–30%) doped with different Cr^{3+} concentrations show that there is a significant difference between the low and high Cr^{3+} concentration doped samples in the position and shape of the emission peaks. When the concentration (x) is lower than 10%, the PL spectra contain both sharp and broadband emission; when the concentration (x) is higher than 14%, only a broadband NIR emission peak is observed. In addition, there is a greater redshift of 95 nm (715 nm → 810 nm) with increasing doping concentration. And the FWHM is

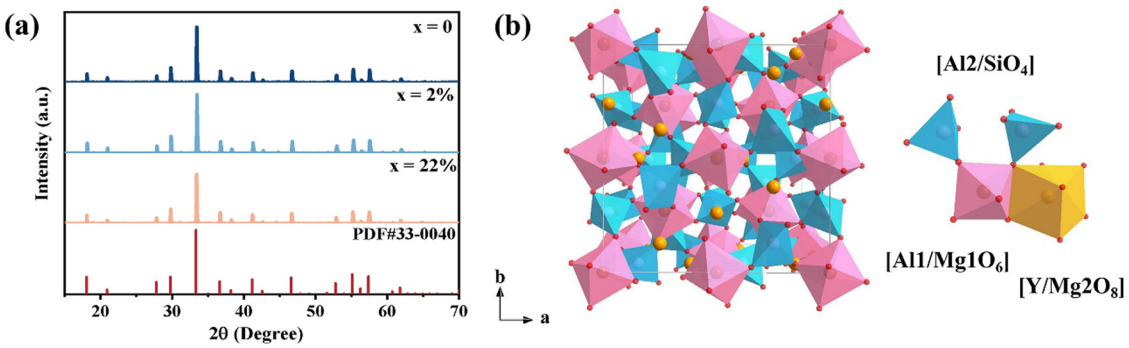

Fig. 1 (a) XRD patterns of YMAS:xCr^{3+} (x = 0, 2% and 22%). (b) The structural model of YMAS.

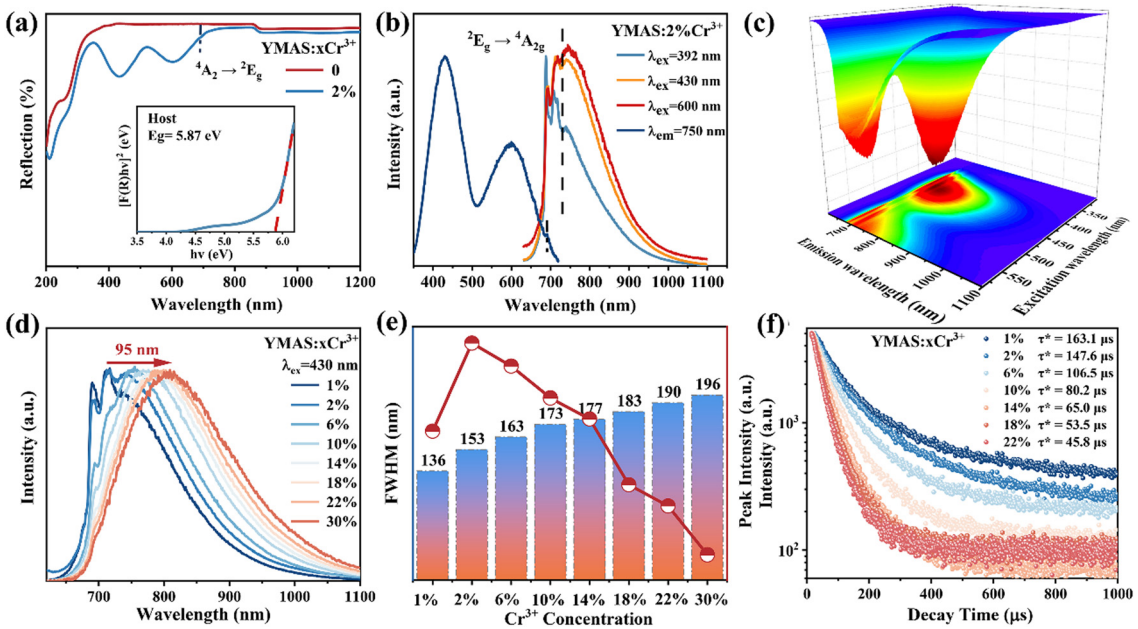

Fig. 2 (a) UV-vis-NIR DR spectra of YMAS:xCr^{3+} (x = 0, 2%). The illustration is the optical band gap of the YMAS host. (b) PL and PLE spectra of YMAS:2%Cr^{3+}. (c) The PL mapping spectrum of YMAS:2%Cr^{3+}. (d) Normalized PL spectra of YMAS:xCr^{3+} (x = 1–30%). (e) Luminescence peak intensity and FWHM of YMAS:xCr^{3+} (x = 1–30%). (f) Fluorescence decay curves of YMAS:xCr^{3+} (x = 1–22%) at the optimal monitoring wavelength (715–810 nm).

significantly expanded from 136 nm (x = 1%) to 196 nm (x = 30%), as shown in Fig. 2e. Such significant changes in the PL spectra are mainly due to the multi-site occupation of Cr^{3+}, and the details will be discussed in the low-temperature spectra. According to the experimental results, the optimal concentration is determined to be 2%, the IQE of which is as high as 79% (Fig. S2, ESI†). It is worth mentioning that when the doping concentration exceeds 14%, the emission intensity of the sample decreases sharply; at the same time, the luminescence of the sharp line is almost undetectable. Obviously, there is energy transfer (ET) from the strong crystal field luminescence center to the weak crystal field luminescence center.[33]

Fig. 2f shows the luminescence decay curves of YMAS:xCr^{3+} (x = 1% ~ 22%) samples monitored at the corresponding emission wavelengths (715–810 nm, Table S1, ESI†), which can be calculated by the double exponential decay model, as follows:[34]

$$I_t = I_0 + A_1 e^{(-t/\tau_1)} + A_2 e^{(-t/\tau_2)} \quad (1)$$

where, I_0 and I_t represent the PL intensity at the initial moment and t moment, A_1 and A_2 are constant parameters, and τ_1 and τ_2 are the decay time of the double-exponential fitting. The average decay times (τ^*) can be obtained by the following empirical equation:[34]

$$\tau^* = (A_1\tau_1^2 + A_2\tau_2^2)/(A_1\tau_1 + A_2\tau_2) \quad (2)$$

Fig. 2f shows the calculated τ^* value of Cr^{3+} in YMAS:xCr^{3+}, and the lifetimes of Cr^{3+} in YMAS are in the microsecond range. The well-fitted double-exponential characteristics and the significant difference between τ_1 and τ_2 (Table S1, ESI†) indicate that there are two luminescent centers in YMAS:xCr^{3+} phosphors.

In particular, the measurement of the spectra at extremely low temperatures can not only greatly reduce the lattice vibration, but also represent the intrinsic emission of the phosphor, which helps to accurately allocate energy levels.[35–37] The PL spectra of YMAS:2%Cr^{3+} at 7 K are shown in Fig. 3a (λ_{ex} = 600 nm) and Fig. S3a (λ_{ex} = 430 nm, ESI†). Fig. 3a shows the NIR emission in the range of 650–1000 nm, consisting of three sharp peaks and a weak broadband emission, which is different from the PL spectrum at RT. The three sharp emission peaks are located at 691 nm, 709 nm and 734 nm, respectively, and the peak at 691 nm is dominant. Whereas the broadband emission near 800 nm is weak. It should be noted that the sharp and broadband emission peaks may come from two different luminescence centers. For this purpose, 691 nm, 709 nm, 734 nm and 850 nm light are selected for monitoring the wavelength and the PLE spectra at 7 K are obtained (Fig. 3b). The peak positions of excitation spectra detected by the three sharp peaks are similar and there is no significant difference. However, the peak position of the excitation spectrum at the detection wavelength of 850 nm has a significant redshift. The excitation peaks at different positions further prove that the two types of emission peaks come from two different luminescent centers.

Combined with the crystal structure, there are three different cation sites [Al1O$_6$], [Mg1O$_6$] and [Al2O$_4$] in the YMAS host, which is suitable for Cr^{3+} occupation. The peaks at 690 nm are zero-phonon R line emission ($^2E_g \rightarrow {}^4A_{2g}$ transition),[38] which represents Cr^{3+} in the unperturbed six-coordinate octahedral crystal field environment, usually indicating a strong crystal field. The lines at 709 nm and 734 nm denoted by (*) in Fig. 3a are Stokes phonon sidebands.[39] Based on the principle of the crystal field, the short ion radius usually results in a strong crystal field environment. Therefore, the sharp peak emission should come from Cr^{3+} in the occupied [Al1O$_6$] octahedron

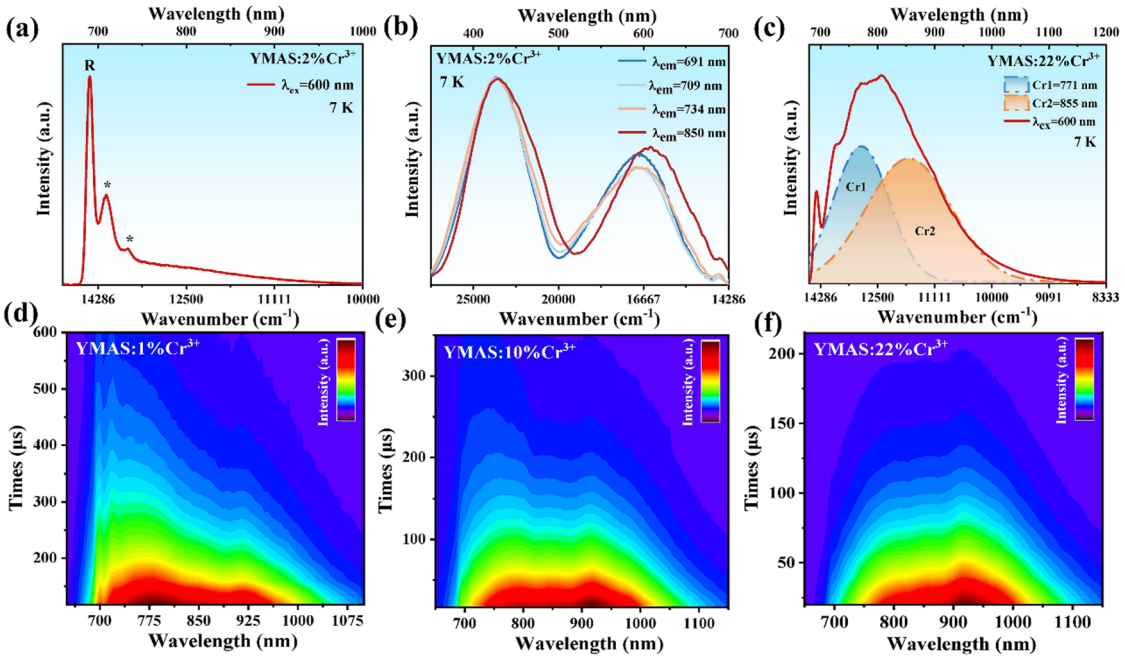

Fig. 3 (a) The PL spectrum, (b) the PLE spectra of YMAS:2%Cr^{3+}, and (c) the PL spectrum of YMAS:22%Cr^{3+} at 7 K. The TRS images of (d) YMAS:1%Cr^{3+}, (e) YMAS:10%Cr^{3+}, and (f) YMAS:22%Cr^{3+}.

(denoted as Cr1). Additionally, there are two possibilities for broadband emission of Cr^{3+}. One is that Cr^{3+} ions locate at the octahedral position with the $^4T_2 \rightarrow {}^4A_2$ spin-allowed transition (Fig. S4a, ESI†).[40] The second is that Cr^{3+} occupies the tetrahedral position with the $^4T_1 \rightarrow {}^2T_1$ spin-allowed transition (Fig. S4b, ESI†).[26,33,41,42] Therefore, both [$Mg1O_6$] and [$Al2O_4$] are likely to be occupied by Cr^{3+} to form the broadband emission near 850 nm (denoted as Cr2).

In addition, the emission spectrum dominated by the sharp peak emission (7 K, Fig. 3a) gradually transforms into the broadband emission (RT, Fig. 2b) with increasing temperature, which is mainly attributed to thermal activation. At 7 K, the ^2E (spin-forbidden transition, sharp peak emission) state is the lowest excited state of Cr^{3+}, while the $^4T_2$ (spin-allowed transition, broadband emission) state is the higher state, and the PL spectrum is dominated by spikes. As the temperature increases, the probability of electrons in Cr^{3+} ions transitioning from the ^2E state to the $^4T_2$ state increases, resulting in more electrons being thermally occupied at the $^4T_2$ state,[43] which in turn causes the intensity of broadband emission to gradually increase. Therefore, broadband emission dominates the PL spectrum at RT.

In order to explore the reasons for emission peak redshift and the increase of FWHM, the intrinsic emission spectrum at high doping concentration is further measured. The emission spectra of YMAS:22%Cr^{3+} at 7 K are measured and shown in Fig. 3c (λ_{ex} = 600 nm) and Fig. S3b (ESI†) (λ_{ex} = 430 nm, ESI†). Different from the emission spectrum dominated by spikes at low doping concentrations, the PL spectrum of YMAS:22% Cr^{3+} is dominated by the broadband emission, and can also be fitted by Gaussian to synthesize two broadband (Fig. 3c). With the increase of substitution amount, the distortion of [$Al1O_6$] octahedron caused by larger Cr^{3+} replacing smaller Al^{3+} increases, and the structural disorder is enhanced, which leads to the decrease of crystal field strength. Therefore, the gradual transition of sharp peak emission (Cr1) into broadband emission at high concentration is one of the reasons causing the red shift of emission peak and the increase of FWHM. Another reason is that the proportion of Cr2 with long wavelength and broadband emission is gradually increasing.

The two Cr^{3+} emission centers and their interactions are further supported by TRS analysis.[39] Fig. 3d shows the TRS image of YMAS:1%Cr^{3+} at 0–600 μs time interval under 430 nm pulse Xe lamp excitation. Cr1 ions are in charge of the sharp and broadband emission, covering 650–840 nm. Cr2 only contributes to the broadband emission, covering the NIR range of 840–1100 nm. In Fig. 3d, it can be observed that the lifetime of Cr1 is longer than Cr2. However, with the increase of concentration (x), the lifetime of Cr1 is shorter than Cr2 (Fig. 3f), which means that Cr1 is more easily quenched by concentration.

Here, the assignment of long-wavelength broadband emission (Cr2) is still uncertain: Cr^{3+} occupying [$Mg1O_6$] or [$Al2O_4$]? Therefore, a novel design method of a site elimination strategy is proposed. According to the radius matching principle, [$Al1O_6$]–[$Al2O_4$] are introduced to replace [$Mg1O_6$]–[SiO_4] without drastic changes in the structure. When [$Mg1O_6$] is completely eliminated, the chemical formula is $Y_2MgAl_4SiO_{12}$ (YMA_4S). The remaining Mg ions and Y ions form the dodecahedron in the YMA_4S structure since large ions reside in a large polyhedral volume position in the garnet structure.[44] If Cr^{3+} occupies [$Al1O_6$] and [$Mg1O_6$] sites in the original YMAS host, after the elimination of the [$Mg1O_6$] octahedron, the emission spectrum would be composed of only one luminescent center. If the emission spectrum still has two luminescent centers as before

substitution, Cr^{3+} would occupy the [Al1O_6] and [Al2O_4] polyhedron.

Furthermore, the phase stability of YMAS ($Y_2Mg_{2-y}Al_{2+2y}Si_{2-y}O_{12}$, y = 0) and YMA$_4$S ($Y_2Mg_{2-y}Al_{2+2y}Si_{2-y}O_{12}$, y = 1) is confirmed by the tolerance factor (D_τ) which is used to predict and analyze the phase stability of the $(A)_3\{B\}_2[C]_3O_{12}$ garnet structure. For real garnet-based compounds, the D_τ value should fluctuate around 1, in the range of 0.748–1.333. The calculation formula of D_τ is as follows:[44]

$$D_\tau = \frac{3\sqrt{(R_B + R_O)^2 - \frac{4}{9}(R_A - R_O)^2}}{2(R_C + R_O)} \quad (3)$$

Where D_τ is the tolerance factor. R_A, R_B and R_C are the ionic radius values of dodecahedron, octahedron and tetrahedron in the garnet structure, respectively. And R_O is the ionic radius value of O^{2-}. By calculation, the D_τ value of the $Y_2Mg_{2-y}Al_{2+2y}Si_{2-y}O_{12}$ is 1.116 for y = 0 (YMAS) and 0.952 for y = 1 (YMA$_4$S) is closer to 1, which means that the phase is more stable after the [MgO_6] octahedron is completely eliminated. It shows that the site elimination strategy is feasible.

3.3. Site elimination strategy

The XRD patterns of $Y_2Mg_{2-y}Al_{2+2y}Si_{2-y}O_{12}$:2%$Cr^{3+}$ (y = 0.1, 0.5 and 1) powder samples are shown in Fig. S5 (ESI†). With the increase of y value, the standard card of the matched diffraction peak is still PDF #33-0040, indicating that the $Y_2Mg_{2-y}Al_{2+2y}Si_{2-y}O_{12}$ solid solutions were successfully synthesized and did not cause dramatic changes in the crystal structure.

The DR spectra of $Y_2Mg_{2-y}Al_{2+2y}Si_{2-y}O_{12}$:$x$$Cr^{3+}$($x$ = 0, 2%; y = 0, 0.5 and 1) are shown in Fig. 4a. According to the formula in eqn (S1) and (S2) (ESI†), the E_g of $Y_2Mg_{2-y}Al_{2+2y}Si_{2-y}O_{12}$:2%$Cr^{3+}$ is 5.25 eV (y = 0), 5.17 eV (y = 0.5) and 4.81 eV (y = 1), respectively, as listed in Fig. 4b. The co-substitution of [Al^{3+}–Al^{3+}] pairs gradually reduce the optical band gap, which means that the introduction of [Al^{3+}–Al^{3+}] pairs induce the rearrangement of electrons in the host. This is because of the different electronegativity between [Al^{3+}–Al^{3+}] and [Mg^{2+}–Si^{4+}] ion pairs.[45]

Fig. 4c shows the PL spectra of $Y_2Mg_{2-y}Al_{2+2y}Si_{2-y}O_{12}$:2%$Cr^{3+}$ (y = 0–1). With the gradual increase of the substitution amount, it can be observed that the emission peak of the R line at 690 nm increases sharply under the excitation of 433 nm light. This means that the introduction of [Al^{3+}–Al^{3+}] co-substituted [Mg^{2+}–Si^{4+}] increases the order of the lattice, and results in the enhancement of the [Al1O_6] octahedral crystal field strength where it is occupied by Cr1. In the process of gradually eliminating the [Mg1O_6] octahedron, the emission spectrum is still broadband emission, and the broadband intensity except the R line does not change much, indicating that the introduction of [Al^{3+}–Al^{3+}] with different electronegativity has little effect on the broad emission band. Even though the [Mg1O_6] octahedron is completely eliminated (y = 1, YMA$_4$S), the broadband emission remains virtually unchanged. The intensity of the broadband emission seems to be less affected by the crystal field strength, which indicates that YMA$_4$S:2%Cr^{3+} still has two luminescent centers, and also confirms that Cr2 is located in the tetrahedral (Al2O_4) position rather than the octahedron (Mg1O_6).

To further measure the composition of YMA$_4$S, the content of the YMA$_4$S:2%Cr^{3+} sample is measured by inductively coupled plasma mass spectrometry (ICP-MS) and the results are given in Table S2 (ESI†). According to the measurement

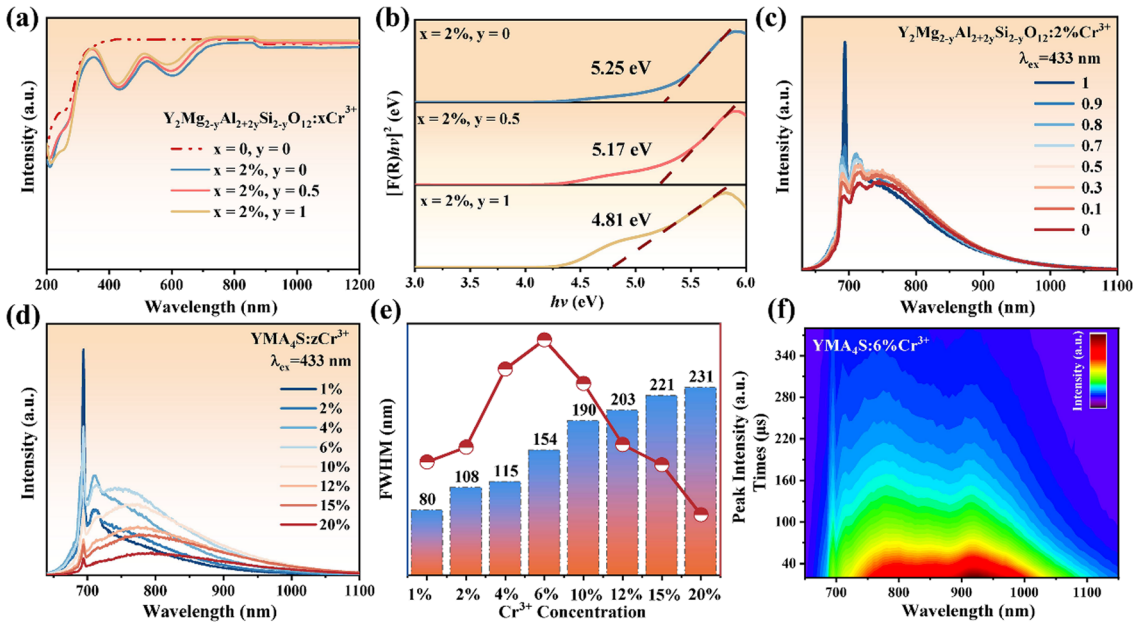

Fig. 4 (a) UV-vis-NIR DR spectra of $Y_2Mg_{2-y}Al_{2+2y}Si_{2-y}O_{12}$:$x$$Cr^{3+}$ (x = 0, 2%; y = 0, 0.5 and 1). (b) The optical band gap of $Y_2Mg_{2-y}Al_{2+2y}Si_{2-y}O_{12}$:2%$Cr^{3+}$ (y = 0, 0.5 and 1). (c) PL spectra of $Y_2Mg_{2-y}Al_{2+2y}Si_{2-y}O_{12}$: 2%Cr^{3+} (y = 0–1). (d) PL spectra of YMA$_4$S:$z$$Cr^{3+}$ (z = 1–20%). (e) Luminescence peak intensity and FWHM of YMA$_4$S (y = 1):$z$$Cr^{3+}$ (z = 1–20%). (f) The TRS image of YMA$_4$S (y = 1):6%Cr^{3+}.

results, the chemical formula is $Y_{2.03}Mg_{0.91}Al_{3.4}SiO_{12}$:1.5%$Cr^{3+}$. However, it is necessary to dilute a higher multiple before testing, which will lead to some test errors.

Fig. S6 (ESI†) shows the Rietveld refinement results for typical $Y_2Mg_{2-y}Al_{2+2y}Si_{2-y}O_{12}$:2%$Cr^{3+}$ (y = 0 and 1) samples. Cr^{3+} ions are constrained to the Al1 and Al2 positions in the Rietveld refinement process. In Tables S3 and S4 (ESI†), the atom positions, occupations, and thermal vibration parameters were improved by convergence and accorded well with the reflection conditions: R_{wp} = 8.96%, R_p = 7.52% for y = 0 and R_{wp} = 9.53%, R_p = 8.72% for y = 1. The YMAS:2%Cr^{3+} is confirmed to be a trigonal Ia-3d structure for the unit cell parameters of $a = b = c$ = 11.967 Å, V = 1713.69 Å^3, $\alpha = \beta = \gamma = 90°$. And the lattice parameters for YMA_4S:2%Cr^{3+} are calculated to be $a = b = c$ = 11.953 Å, V = 1707.78 Å^3. The decrease of the refined volume suggests that [Al1O_6]–[Al2O_4] successfully replaces [Mg1O_6]–[SiO_4] after the site elimination strategy, resulting in a decrease in cell parameters. Reliable refinement results confirm that Cr ions occupy both [Al1O_6] and [Al2O_4] sites.

The ^{27}Al solid-state nuclear magnetic resonance (ss-NMR) spectra of YMAS:$x$$Cr^{3+}$ (x = 0 and 22%) samples shown in Fig. S7 (ESI†) provide direct evidence of Cr^{3+} ions entering the local structure of the [Al2O_4] tetrahedron and [Al1O_6] octahedron. The ^{27}Al ss-NMR spectrum of the Cr^{3+} undoped YMAS sample shows two bands from −30 to +25 ppm and 50 to 100 ppm, corresponding to the [Al1O_6] and [Al2O_4] sites in the garnet structure.[46] After Cr^{3+} doping, the ^{27}Al ss-NMR peaks of the YMAS:22%Cr^{3+} sample are broadened, indicating that the simultaneous entry of Cr^{3+} ions into the [Al2O_4] and [Al1O_6] polyhedron destroys the local symmetry.

To further verify that Cr^{3+} occupies two sites of [Al1O_6] and [Al2O_4], a series of samples of YMA_4S (y = 1):$z$$Cr^{3+}$ (z = 1–20%) are prepared. The corresponding PL spectra show pronounced redshift and broadening of the emission bands (Fig. 4d and e), which is consistent with YMAS:$x$$Cr^{3+}$. Besides, the concentration quenching of YMA_4S (y = 1):$z$$Cr^{3+}$ is observed until z = 6%, which is higher than that of YMAS (y = 0):$x$$Cr^{3+}$ (x = 2%). The reason is that the substitution of [Al1O_6]–[Al2O_4] for [Mg1O_6]–[SiO_4] produces more sites suitable for Cr^{3+} occupation, which extends the concentration quenching value from 2% (YMAS, y = 0) to 6% (YMA_4S, y = 1). The TRS plot of YMA_4S (y = 1):6%Cr^{3+} (Fig. 4f) is very similar to that of YMAS (y = 0): 10%Cr^{3+} (Fig. 3e). Two luminescence centers are still observed in YMA_4S (y = 1):6%Cr^{3+} without the [Mg1O_6] octahedron, and lifetime values of Cr1 is still longer than Cr2 in YMA_4S (y = 1), which is also consistent with YMAS (y = 0). Fig. S8a and b (ESI†) are the luminescence decay curve of two luminescence centers in the YMA_4S:$x$$Cr^{3+}$ (x = 2–15%) samples. In Fig. S8c (ESI†), the different decay rates of Cr1 and Cr2 can be clearly observed. The Cr2 lifetime is short but the attenuation rate is slow, and for Cr1 is the opposite. This means that Cr1 is more easily quenched by concentration. Until then, ample experimental evidence proves that Cr2 should be the emission of Cr^{3+} occupying the [Al2O_4] polyhedron.

3.4. High-temperature thermal stability

Fig. 5a and b show the PL spectra of YMAS:2%Cr^{3+} and YMAS:22%Cr^{3+} excited with 430 nm light at different temperatures, respectively. The emission intensity of both phosphors decreases with increasing temperature, but the decrease for the

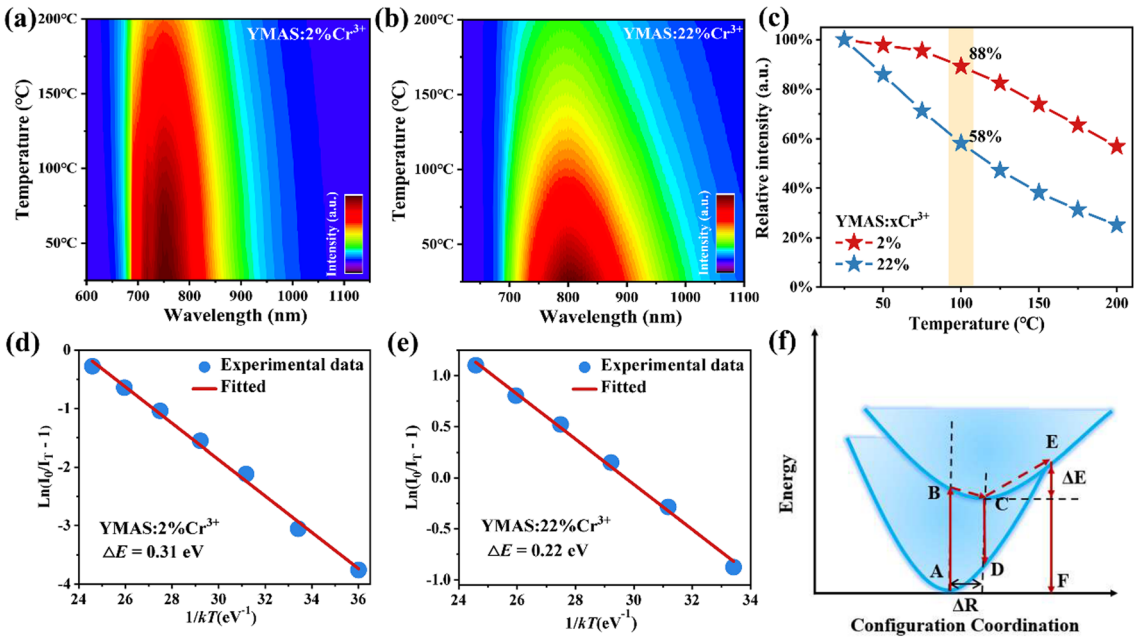

Fig. 5 Temperature-dependent PL spectra of (a) YMAS:2%Cr^{3+} and (b) YMAS:22%Cr^{3+}. (c) Temperature-dependent integral intensity of YMAS:2%Cr^{3+} and YMAS:22%Cr^{3+}. Plot of $\ln(I_0/I_T - 1)$ *versus* $1/kT$ of (d) YMAS:2%$Cr^{3+}$and (e) YMAS:22%Cr^{3+}. (f) Configurational coordinate diagram illustrating band broadening and thermal quenching behaviors of YMAS:$x$$Cr^{3+}$.

YMAS:22%Cr^{3+} phosphor is significantly greater than that for the YMAS:2%Cr^{3+} phosphor. Fig. 5c presents the change in the relative intensity of the emission peaks of YMAS:$x$$Cr^{3+}$ (x = 2%, 22%) as a function of temperature. The integral intensities of these samples remain 88%@100 °C (x = 2%) and 58%@100 °C (x = 22%) of that at RT, respectively, indicating excellent thermal stability of YMAS:2%Cr^{3+}. In order to further explain the TQ behavior, the activation energy (ΔE) of YMAS:$x$$Cr^{3+}$ (x = 2%, 22%) is the energy (ΔE) of YMAS:$x$$Cr^{3+}$ (x = 2%, 22%) and is calculated by the Arrhenius formula:[47,48]

$$I_T = \frac{I_0}{1 + A\exp\left(\frac{-\Delta E}{kT}\right)} \quad (4)$$

where, I_T is the luminous intensity at temperature T, I_0 is the original intensity, A is a constant, and k is 8.617 × 10^{-5} eV K^{-1} (Boltzmann constant). The calculated ΔE = 0.31 eV for YMAS:2%Cr^{3+} and ΔE = 0.22 eV for YMAS:22%Cr^{3+} are shown in Fig. 5d and e.

In the YMAS host, the larger E_g (5.87 eV, as shown in Fig. 2a) inhibits the possibility that the excited electrons are further pumped into the conduction band of the host lattice by thermal energy and then undergo non-radiative recombination with the photooxidation luminescence center or are trapped by some traps in the host.[49] However, the thermal stability of the YMAS:22%Cr^{3+} sample is not excellent. Thus, thermal ionization is not the dominant reason for the good thermal stability of YMAS:2%Cr^{3+}. So why does YMAS:2%Cr^{3+} have better thermal stability, much higher than that of YMAS:22%Cr^{3+}? There are two main reasons: (1) the electron–phonon coupling generates cross-relaxation, and electron returns from the excited state to the ground state through nonradiative transitions rather than radiative transitions, in which the energy barrier required to cause nonradiative transitions is ΔE, as shown in Fig. 5f. Whereas ΔE = 0.31 eV (YMAS:2%Cr^{3+}) is larger than ΔE = 0.22 eV (YMAS:22%Cr^{3+}). It is difficult for the electrons in YMAS:2%Cr^{3+} to cross the energy barrier, and the amount of energy dissipated in the form of thermal energy through nonradiative leaps is reduced. (2) In heavily doped materials, the distance between Cr^{3+} ions is shorter. The increase in temperature enhances the lattice vibration, which promotes the non-radiative relaxation and increases the possibility of the energy transfer process between Cr^{3+} ions, making it easier for photons to enter the killing centers. Therefore, the thermal stability of lightly doped YMAS:2%Cr^{3+} is better.

In addition, Fig. S9a–e (ESI†) shows the PL spectra of $Y_2Mg_{2-y}Al_{2+2y}Si_{2-y}O_{12}$:2%$Cr^{3+}$ (y = 0, 0.1, 0.5, 0.9 and 1) excited with 430 nm light at different temperatures, respectively. Their corresponding emission intensities show the same decreasing trend with increasing temperature. The integral intensities of all samples can be maintained more than 80%@100 °C room temperature, as shown in Fig. S9f (ESI†). Among them, YMA_4S:2%Cr^{3+} exhibits the most excellent thermal stability (92%@100 °C).

3.5. Applications

To further evaluate the application potential of YMAS:Cr^{3+} phosphors, pc-LED was fabricated using YMAS:2%Cr^{3+} and a commercial 460 nm blue chip (insert in in Fig. 6a). Fig. 6a shows the PL spectral increment curve of the pc-LED device. As the driving current increases from 50 to 300 mA, the spectral

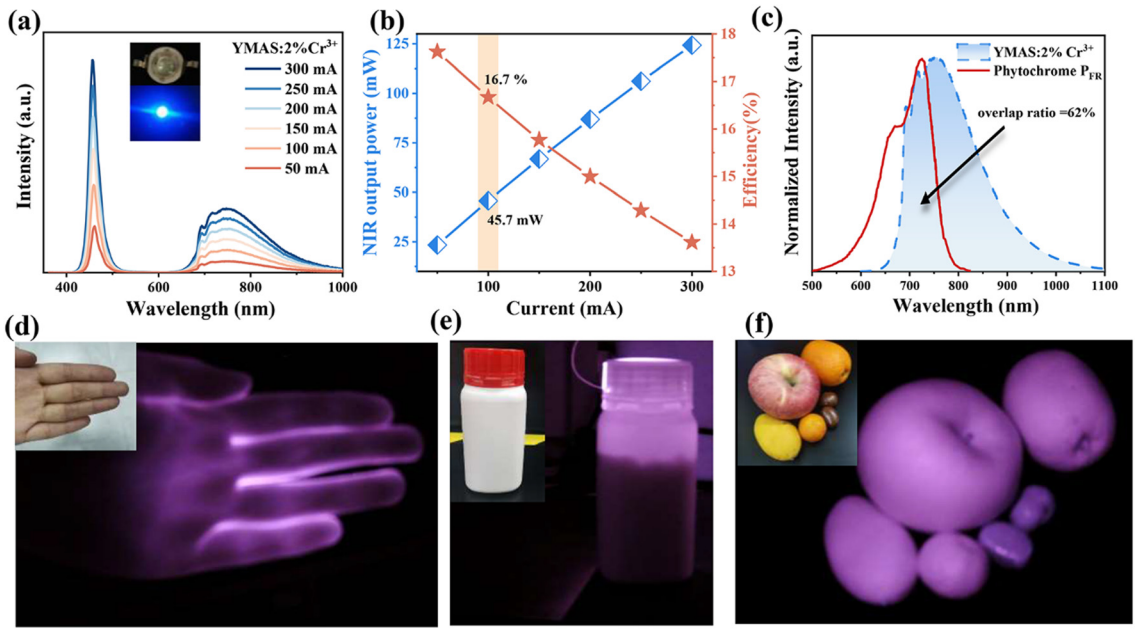

Fig. 6 (a) Luminescence spectra of the as-fabricated NIR pc-LED lamp at different drive currents. The inset shows the working and nonworking state of the device. (b) The output power of NIR light and photoelectric conversion efficiency dependent on the driving current. (c) The overlap rate of the emission spectrum with P_{FR}. The practical application performance of the fabricated NIR pc-LED lamp in (d) bioimaging, (e) non-destructive testing, and (f) night vision.

intensity continues to increase without saturation. Fig. 6b presents the photoelectric characteristics test results of NIR pc-LED, which indicates a gradual increase in output power at the cost of reduced photoelectric efficiency. Under a forward current of 100 mA, the output power and photoelectric efficiency of the NIR pc-LED prepared by the YMAS:2%Cr^{3+} phosphor are 45.7 mW and 16.7%, respectively. By comparing the reported Cr^{3+}-doped garnet-type luminescent materials (Table 1), the photoelectric performance of NIR pc-LED prepared by YMAS:2%Cr^{3+} is more desirable for application.

Fig. 6c compares the emission spectrum of YMAS:2%Cr^{3+} and the absorption spectrum of plant phytochrome P_{FR}.[50–52] The spectral similarity index is calculated to be 62% by quantitative analysis, which indicates that the material could effectively promote plant growth and mainly play a role in regulating phytochrome P_{FR}. In addition, its practical performance in bioimaging, non-destructive testing and night vision is also explored. NIR light from an LED can penetrate the palms and fingers, and can see the bones clearly (Fig. 6d). Under the illumination of the prepared pc-LED device, the drug allowance can be clearly observed in the dark environment with the help of a NIR camera, which means that it also has a good application prospect in non-destructive testing (Fig. 6e). Finally, in the dark environment, with the help of NIR light, different kinds of fruits and foods can be clearly distinguished, indicating that it also has a good application prospect in night vision (Fig. 6f).

4. Conclusions

In this work, a series of YMAS:Cr^{3+} NIR-emitting phosphors were successfully developed and synthesized. The broadband NIR emission accompanied by sharp peak emission is obtained due to the occupation of two different luminescent centers of Cr^{3+} in the YMAS lattice. Benefiting from the site elimination strategy, the double luminescent centers are proven to be derived from the two sites of [$Al1O_6$] (Cr1) and [$Al2O_4$] (Cr2). It provides a new design idea for studying the occupation of different lattice sites of doped ions. Moreover, YMAS:2%Cr^{3+} has an excellent quantum efficiency (79%) and thermal stability ($\approx$ 88%@100 °C). The NIR output power and photoelectric conversion efficiency of the NIR packaging material prepared using YMAS:2%Cr^{3+} are as high as 45.7 mW@100 mA and 16.7%@100 mA, respectively. Owing to the excellent performance of the YMAS:2%Cr^{3+} sample, the as-fabricated NIR device exhibits potential application performance in plant growth, bioimaging, non-destructive testing and night vision.

Conflicts of interest

There are no conflicts to declare.

Acknowledgements

This work was financially supported by the National Natural Science Foundation of China (NSFC No. 12374376 and 12304461), the Natural Science Foundation of Shandong Province (ZR2021ZD10), and the Project of the Qilu Young Scholar Program of Shandong University.

References

1 Y. Liang, Q. Cao, Y. Zhou, W. Zhou, J. Zhang, L. Yu, S. Lian and Z. Qiu, *Chem. Eng. J.*, 2023, **454**, 140235.
2 S. Mura, C. Cappai, G. F. Greppi, S. Barzaghi, A. Stellari and T. M. P. Cattaneo, *Comput. Electron. Agric.*, 2019, **159**, 92.
3 J. Wang, X. Wang, C. Zhang, X. Zhang, T. Zhou and R.-J. Xie, *J. Mater. Chem. C*, 2023, **11**, 9030–9036.
4 Z. Chang, W. Deng, X. Ren, X. Liu, G. Luo, Y. Tan, X. Zhang and J. Jie, *ACS Appl. Mater. Interfaces*, 2023, **15**, 32037.
5 J. Meng, Y. Cui and Y. Wang, *J. Mater. Chem. B*, 2022, **10**, 8596.
6 H. Jiang, L. Liu, K. Yu, X. Yin, S. Zheng, L. Song, J. Shi and Y. Zhang, *J. Rare Earths*, 2022, **40**, 1389.
7 R. Li, G. Wei, Z. Wang, Y. Wang, J. Li, S. He, L. Li, H. Suo, W. Ding and P. Li, *Laser Photonics Rev.*, 2023, **17**, 2200589.
8 Y. Wang, M. Shang, Y. Sun, M. Deng, X. Xing, P. Dang and J. Lin, *J. Mater. Chem. C*, 2023, **11**, 9291–9299.
9 M. M. Nagy, S. Wang and M. A. Farag, *Trends Food Sci. Technol.*, 2022, **123**, 290.
10 H. Suo, Y. Wang, X. Zhao, X. Zhang, L. Li, K. Guan, W. Ding, P. Li, Z. Wang and F. Wang, *Laser Photonics Rev.*, 2022, **16**, 2200012.
11 G. B. Nair, H. C. Swart and S. J. Dhoble, *Prog. Mater. Sci.*, 2020, **109**, 100622.
12 Y. Shi, Z. Wang, J. Peng, Y. Wang, S. He, J. Li, R. Li, G. Wei, Y. Yang and P. Li, *Mater. Today Adv.*, 2022, **16**, 100305.
13 R. Li, Y. Liu, C. Yuan, G. Leniec, L. Miao, P. Sun, Z. Liu, Z. Luo, R. Dong and J. Jiang, *Adv. Opt. Mater.*, 2021, **9**, 2100388.
14 Y. Sun, M. Shang, Y. Wang, Y. Zhu, X. Xing, P. Dang and J. Lin, *Ceram. Int.*, 2023, **49**, 32619.
15 Z. Jia, C. Yuan, Y. Liu, X.-J. Wang, P. Sun, L. Wang, H. Jiang and J. Jiang, *Light: Sci. Appl.*, 2020, **9**, 86.
16 Q. Shao, H. Ding, L. Yao, J. Xu, C. Liang and J. Jiang, *RSC Adv.*, 2018, **8**, 12035.
17 X. Xu, Q. Shao, L. Yao, Y. Dong and J. Jiang, *Chem. Eng. J.*, 2020, **383**, 123108.
18 Y. Yan, M. Shang, S. Huang, Y. Wang, Y. Sun, P. Dang and J. Lin, *ACS Appl. Mater. Interfaces*, 2022, **14**, 8179.
19 S. Liu, Y. Zheng, D. Peng, J. Zhao, Z. Song and Q. Liu, *Adv. Funct. Mater.*, 2023, **33**, 2209275.
20 M. Zhao, S. Liu, H. Cai, F. Zhao, Z. Song and Q. Liu, *Sci. China Mater.*, 2022, **65**, 748–756.
21 S. Wu, H. Liang, Y. Li, W. Zou, Z. Liao, W. Wang and X. Ye, *Dalton Trans.*, 2023, **52**, 6569.
22 Y. Jin, Z. Zhou, R. Ran, S. Tan, Y. Liu, J. Zheng, G. Xiang, L. Ma and X. Wang, *Adv. Opt. Mater.*, 2022, **10**, 2202049.
23 T. Xu, L. Yuan, Y. Chen, Y. Zhao, L. Ding, J. Liu, W. Xiang and X. Liang, *Opt. Mater.*, 2019, **91**, 30.
24 C. Wang, X. Wang, Y. Zhou, S. Zhang, C. Li, D. Hu, L. Xu and H. Jiao, *ACS Appl. Electron. Mater.*, 2019, **1**, 1046.

25 X. Zou, H. Zhang, W. Li, M. Zheng, M. S. Molokeev, Z. Xia, Y. Zheng, Q. Li, Y. Liu, X. Zhang and B. Lei, *Adv. Opt. Mater.*, 2022, **10**, 2200882.
26 V. Rajendran, M.-H. Fang, G. N. D. Guzman, T. Lesniewski, S. Mahlik, M. Grinberg, G. Leniec, S. M. Kaczmarek, Y.-S. Lin, K.-M. Lu, C.-M. Lin, H. Chang, S.-F. Hu and R.-S. Liu, *ACS Energy Lett.*, 2018, **3**, 2679.
27 L. Jiang, X. Jiang, L. Zhang, Q. Liu, X. Mi, Z. Yu, G. Lv and Y. Su, *Inorg. Chem.*, 2023, **62**, 4220.
28 L. Wang, Y. Liu, H. Yu, C. Yang, L. Mei, H. Ding and R. Mi, *J. Alloys Compd.*, 2023, **961**, 170745.
29 B. Bai, P. Dang, D. Huang, H. Lian and J. Lin, *Inorg. Chem.*, 2020, **59**, 13481.
30 T. Gao, W. Zhuang, R. Liu, Y. Liu, X. Chen and Y. Xue, *J. Alloys Compd.*, 2020, **848**, 156557.
31 Y. Wang, G. Liu and Z. Xia, *Laser Photonics Rev.*, 2023, 2300717.
32 F. Zhao, Z. Song and Q. Liu, *Laser Photonics Rev.*, 2022, **16**, 2200380.
33 Y. Zhou, C. Li and Y. Wang, *Adv. Opt. Mater.*, 2022, **10**, 2102246.
34 C. Yang, C. Fan, F. Hussain, W. Sheng, K. Song, J. Wu, Q. Huang, W. Su, J. Xu, S. Sun and D. Wang, *J. Rare Earths*, 2023, **41**, 489.
35 V. Rajendran, M.-H. Fang, W.-T. Huang, N. Majewska, T. Lesniewski, S. Mahlik, G. Leniec, S. M. Kaczmarek, W. K. Pang, V. K. Peterson, K.-M. Lu, H. Chang and R.-S. Liu, *J. Am. Chem. Soc.*, 2021, **143**, 19058.
36 H. Lin, G. Bai, T. Yu, M.-K. Tsang, Q. Zhang and J. Hao, *Adv. Opt. Mater.*, 2017, **5**, 1700227.
37 H. Zeng, T. Zhou, L. Wang and R.-J. Xie, *Chem. Mater.*, 2019, **31**, 5245.
38 Q. Zhang, X. Wei, J. Zhou, B. Milićević, L. Lin, J. Huo, J. Li, H. Ni and Z. Xia, *Adv. Opt. Mater.*, 2023, **11**, 2300310.
39 L. Yao, Q. Shao, M. Shi, T. Shang, Y. Dong, C. Liang, J. He and J. Jiang, *Adv. Opt. Mater.*, 2022, **10**, 2102229.
40 L. Jiang, X. Jiang, J. Xie, H. Sun, L. Zhang, X. Liu, Z. Bai, G. Lv and Y. Su, *J. Alloys Compd.*, 2022, **920**, 165912.
41 Z. Song and Q. Liu, *Adv. Theory Simul.*, 2022, **5**, 2200466.
42 T. Wang, Y. Wang, W. Chen and Z. Xia, *Laser Photonics Rev.*, 2023, 2300784.
43 M.-H. Fang, G. N. A. De Guzman, Z. Bao, N. Majewska, S. Mahlik, M. Grinberg, G. Leniec, S. M. Kaczmarek, C.-W. Yang, K.-M. Lu, H.-S. Sheu, S.-F. Hu and R.-S. Liu, *J. Mater. Chem. C*, 2020, **8**, 11013.
44 Z. Song, D. Zhou and Q. Liu, *Acta Crystallogr., Sect. C: Struct. Chem.*, 2019, **75**, 2053–2296.
45 T. Lang, M. Cai, S. Fang, T. Han, S. He, Q. Wang, G. Ge, J. Wang, C. Guo, L. Peng, S. Cao, B. Liu, V. I. Korepanov, A. N. Yakovlev and J. Qiu, *Adv. Opt. Mater.*, 2022, **10**, 2101633.
46 J. Feng, H. Liu, Z. Ma, J. Feng, L. Chen, J. Li, Y. Cai, Q. Zeng, D. Wen and Y. Guo, *Chem. Eng. J.*, 2022, **449**, 137892.
47 H. Liu, F. Zhao, H. Cai, Z. Song and Q. Liu, *J. Mater. Chem. C*, 2022, **10**, 9232.
48 Q. Wang, S. Wang, R. Pang, T. Tan, T. Tan, H. Wen, S. Zhang, H. You, C. Li and H. Zhang, *Mater. Res. Bull.*, 2023, **163**, 112222.
49 G. Liu and Z. Xia, *J. Phys. Chem. Lett.*, 2022, **13**, 5001.
50 S. J. Gai, C. Zhou, L. Peng, M. H. Wu, P. X. Gao, L. J. Su, M. S. Molokeev, Z. Zhou and M. Xia, *Mater. Today Chem.*, 2022, **26**, 101107.
51 X. Zou, X. Wang, H. Zhang, Y. Kang, X. Yang, X. Zhang, M. S. Molokeev and B. Lei, *Chem. Eng. J.*, 2022, **428**, 132003.
52 Y. Zhang, Z. Zeng, G. Li, P. Gao, Y. Li, M. Xia and Z. Zhou, *Spectrochim. Acta, Part A*, 2023, **302**, 123122.